

Hybrid Nanoplatfom: Enabling a Precise Antitumor Strategy via Dual-Modal Imaging-Guided Photodynamic/Chemo-/Immunosynergistic Therapy

Haoran Chen, Fengxia Wu, Xiaoyu Xie, Wang Wang, Qiqing Li, Langping Tu, Bin Li, Xianggui Kong, and Yulei Chang*



Cite This: *ACS Nano* 2021, 15, 20643–20655



Read Online

ACCESS |



Metrics & More



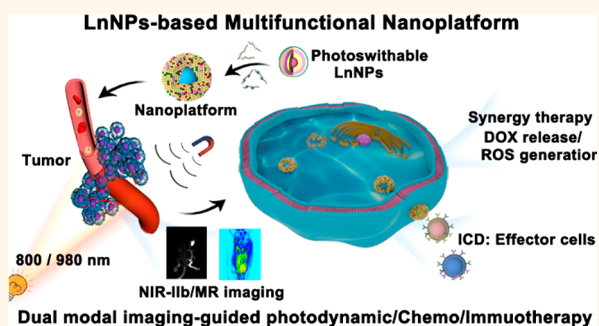
Article Recommendations



Supporting Information

ABSTRACT: Photodynamic therapy (PDT) has been widely used in tumor therapy due to its high spatial–temporal control and noninvasiveness. However, its clinical application is limited by weak efficacy, shallow tissue penetration, and phototoxicity. Herein, a facile theranostic nanoplatfom based on photoswitchable lanthanide-doped nanoparticles was designed. Typically, these nanoparticles had UV–blue and 1525 nm emission upon 980 nm excitation and 1525 nm emission upon 800 nm excitation. We further used these nanoparticles for achieving real-time near-infrared (NIR)-IIb imaging (800 nm) with a high signal-to-noise ratio and imaging-guided PDT (980 nm). Moreover, such a photoswitchable nanoplatfom capping with pH-sensitive calcium phosphate for co-loading doxorubicin (a chemotherapeutic immunogenic cell death [ICD] inducer) and paramagnetic Mn^{2+} ions enhances T_1 -magnetic resonance imaging in the tumor microenvironment. Our results suggest that this theranostic nanoplatfom could not only kill tumor cells directly through dual-modal image-guided PDT/chemotherapy but also inhibit distant tumor and lung metastasis through ICD. Therefore, it has great potential for clinical application.

KEYWORDS: lanthanide-doped nanoparticles, upconversion, photoswitch, photodynamic therapy, theranostics, immunogenic cell death, NIR-IIb imaging guidance



Improving the therapeutic efficiency while reducing the adverse effects of current anticancer therapy is a huge challenge. Photodynamic therapy (PDT) is one of the most promising and widely used cancer therapeutic modalities owing to its low systemic toxicity, high selectivity, and noninvasiveness.^{1,2} This treatment approach involves transforming oxygen into cytotoxic reactive oxygen species (ROS) in cancer cells upon irradiating photosensitizers with a specific light. The generated ROS kills tumor cells via apoptosis or necrosis. PDT-mediated cell death is also associated with an antitumor immune response, termed as immunogenic cell death (ICD),³ which is mainly mediated by the surface exposure of calreticulin (CRT), ATP secretion, and high mobility group protein B1 (HMGB1) release.^{4–6} Antitumor-specific T-cell responses achieve distant tumor suppression. Unfortunately, the therapeutic effect of PDT is confined by shallow penetration,⁷ inappropriate trigger timing, and location, which compromises its therapeutic effects. Treatment

accuracy can be improved by gathering *in vivo* imaging data, which will guide subsequent treatments.^{8–10}

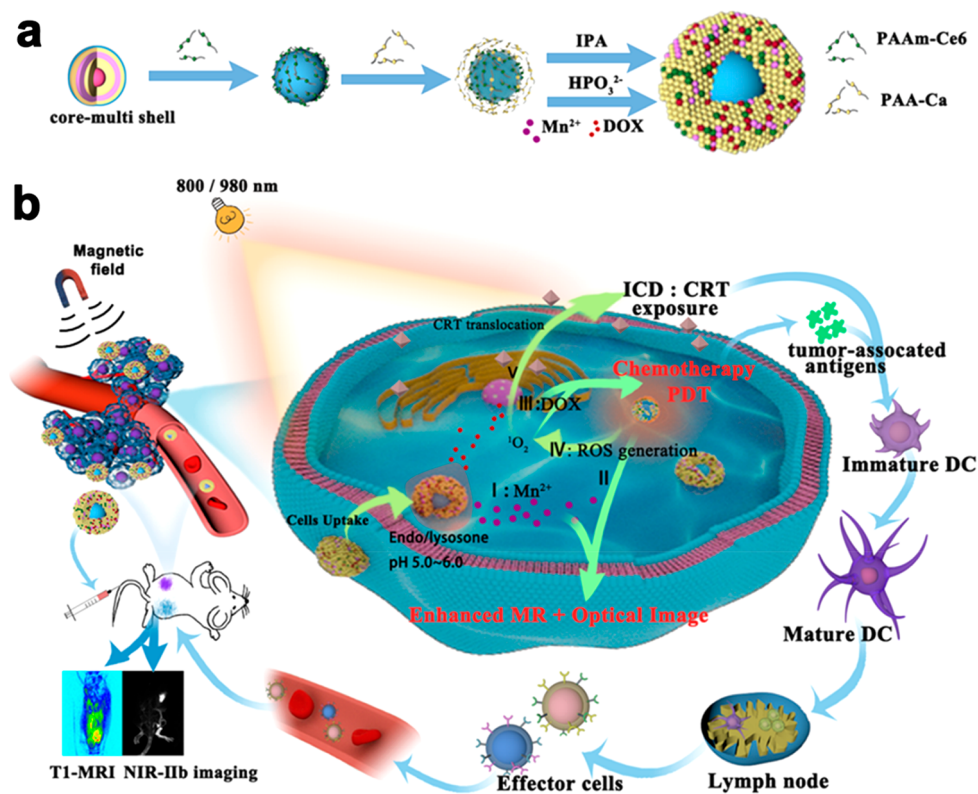
Lanthanide-doped nanoparticles (LnNPs), which can harvest near-infrared (NIR) light to emit higher energy photons (upconversion) or lower energy photons (downshifting), play an important role in photomediated tumor theranostic approaches. Recently, NIR-activated LnNPs-based PDT showing deep tissue penetration,^{11–13} have attracted notable interest for tumor therapy. However, PDT alone cannot achieve satisfactory therapeutic outcomes¹⁴ due to the inherent risks of recurrence and metastasis. Therefore, LnNPs-

Received: October 30, 2021

Accepted: December 6, 2021

Published: December 8, 2021



Scheme 1. Synthesis of Nanoplatform and Functioning Mechanism^a

^a(a) Schematic illustration of the synthesis of nanoplatform. (b) The functioning mechanism, including circulation in blood vessels, imaging, and tumor therapy.

PDT is combined with other therapeutic modalities, thereby amplifying the advantages and offsetting the disadvantages, for instance chemotherapy, chemodynamic therapy, photothermal therapy, and immunotherapy.^{15,16} The combination of PDT with chemotherapeutic drugs has been explored, for example doxorubicin (DOX)^{17,18} and paclitaxel (PTX). These chemotherapeutic drugs also can induce ICD. Such a combination could elicit an immune response cascade to further enhance the antitumor activity and reduce adverse effects.

Besides, LnNPs exhibit excellent magnetic properties and strongly attenuate X-rays, making them useful for multiple imaging methods, for instance optical, magnetic resonance (MR), and computed tomography imaging.^{19–21} Notably, optical imaging is a type of nondestructive, highly sensitive, and quick-responding imaging modality. To date, most PDT-related optical imaging in previous reports only toward the visible and NIR-I radiation, ignoring NIR-II (1000–1700 nm) downshifting one.²² NIR-IIb (1500–1700 nm) effectively reduces autofluorescence, absorption, and light scattering of tissues, achieving deeper penetration and greater image clarity.^{23–25} Therefore, it seems logical to conduct NIR-IIb imaging-guided PDT.²⁶

Nevertheless, the millimeter-level penetration depth of the NIR-II region at micron-scale resolution hinders its application in most clinical settings.²⁷ Thus, it becomes necessary to combine one or two other imaging modalities to obtain [Supporting Information](#), which can further improve the accuracy of diagnosis/imaging.²⁸ Gd³⁺-based LnNPs act as T₁-weighted MRI contrast agents by influencing the relaxation ability of water, providing anatomical details with unlimited penetration depth and superior spatial resolution.²⁹ The

combination of optical imaging with MRI can comprehensively increase diagnostic sensitivity and penetration depth, making it easier to guide subsequent therapy. However, some surface modification methods in fabricating the multifunctional nanoplatform severely limit the exposed amount of Gd³⁺ ions, which inevitably leads to low signal-to-noise ratios of MRI. Although this issue can be overcome by increasing the dose, high dose regimes increase the risk of Gd³⁺ retention and adverse effects *in vivo*. In addition, the exposure of Gd³⁺ ions for better MR contrast can be increased by reducing the nanoparticle size to obtain ideal longitudinal relaxation, but this also decreases the luminescence efficiency. Therefore, to achieve a certain level of MRI contrast for imaging guidance and avoid the potential biological toxicity caused by the high concentration of single paramagnetic ions, it is necessary to introduce other paramagnetic ions (i.e., Mn²⁺ or Fe³⁺). This will enhance the T₁-MRI signal, especially by responding to the tumor microenvironment (TME) to establish the enhanced-MRI nanoplatform with a strong optical signal. Taken together, developing an on-demand theranostic nanoplatform for tumor therapy that combines diagnosis, therapeutics, and immunity would greatly improve the antitumor efficiency while reducing adverse effects.

Herein, we designed a multifunctional theranostic nanoplatform (LnNP-Ce6@CaP/Mn-DOX) for TME-enhanced MR imaging and real-time NIR-IIb (1525 nm) dual-modal imaging-guided synergistic therapy (Photodynamic/Chemo/Immunotherapy), as illustrated in [Scheme 1](#). In this nanoplatform, a stepwise imaging strategy was employed. First, T₁-MRI was carried out to determine the preliminary tumor positioning using paramagnetic Gd³⁺ and Mn²⁺. The idea is that T₁-MRI

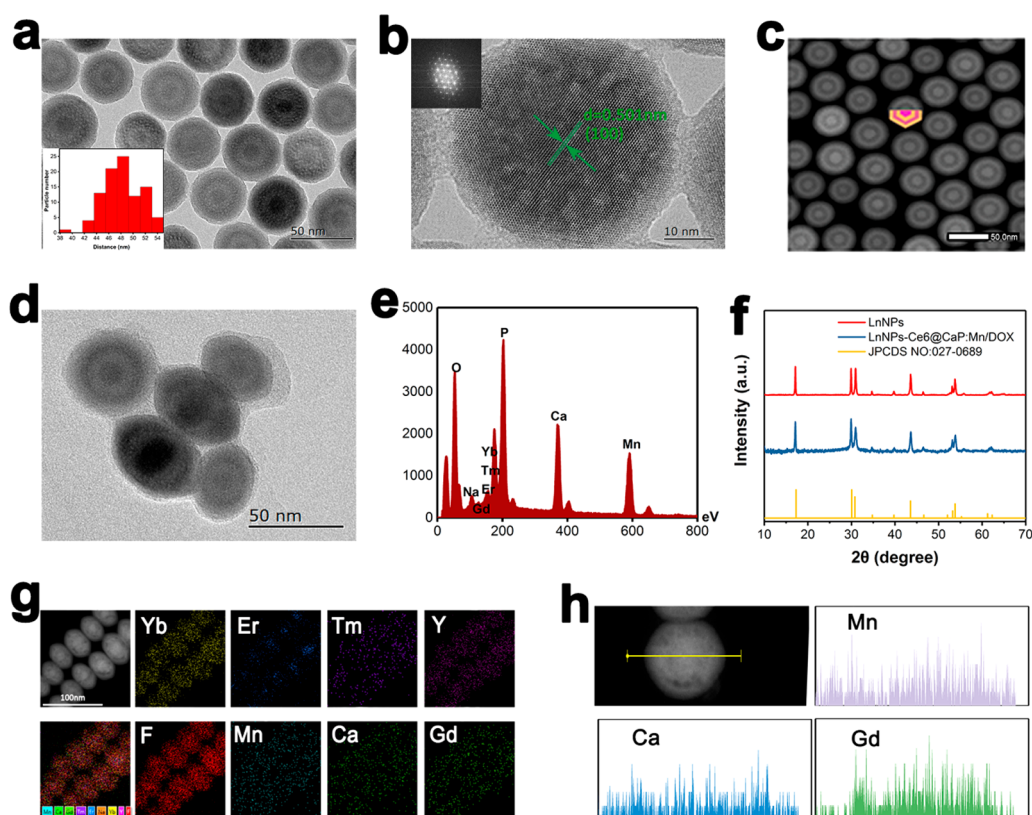


Figure 1. Characterization of LnNPs and LnNP-Ce6@CaP: Mn/DOX. (a) TEM and (b) corresponding high-resolution TEM image of LnNPs. (c) HAADF-STEM image of LnNPs. (d) TEM images of LnNP-Ce6@CaP:Mn/DOX. (e) EDX of LnNP-Ce6@CaP:Mn/DOX. (f) XRD of LnNPs and LnNP-Ce6@CaP:Mn/DOX. (g) HAADF-STEM-EDS mapping image of LnNP-Ce6@CaP:Mn/DOX. (h) Line scans of LnNP-Ce6@CaP:Mn/DOX.

performance would be enhanced once Mn^{2+} ions are released from the calcium phosphate (CaP) layer in the TME/cells, which would increase the interaction between the protons and Mn^{2+} ions to affect water proton relaxation. Subsequently, the tumor was exposed to an 800 nm laser for real-time imaging in NIR-IIb region, which would allow deep tissue bioimaging. After that, photoswitchable PDT was conducted by excitation with 980 nm radiation, which was also guided by the NIR-IIb imaging. Tumor-targeted chemotherapy was achieved when the CaP layer decomposed in the mildly acidic TME/acidic organelles, inducing DOX release, which synergized with PDT to improve the treatment efficacy. The PDT/Chemo synergistic therapy was also associated with an antitumor ICD response. Our results showed significant antitumor and metastasis inhibition effects *in vitro* and *in vivo*. Therefore, a smart theranostic nanoplatform with dual-modal image-guided PDT/chemo combination therapy and the subsequent immune response has immense clinical application potential.

RESULTS AND DISCUSSION

Preparation and Characterization of the Theranostic Nanoplatform. The preparation scheme of the multifunctional theranostic nanoplatform is illustrated in Scheme 1. In this design, the multiwavelength excited Er^{3+} and single-wavelength excited Yb^{3+} and Tm^{3+} were partitioned in multishelled LnNPs ($\text{NaErF}_4:0.5\%\text{Tm}@ \text{NaYF}_4@ \text{NaYbF}_4:0.5\%\text{Tm}@ \text{NaYF}_4@ \text{NaGdF}_4$), which were synthesized through a successive coprecipitation approach for realizing the light-controlled switch. The UV-blue upconversion emissions for fluorescence resonance energy transfer (FRET)-based PDT

upon 980 nm excitation were achieved by codoping Tm^{3+} and Yb^{3+} ions in the second outer layer. A stronger NIR-IIb emission of Er^{3+} at 1525 nm under 800 nm excitation was obtained by introducing 0.5% (mol) Tm^{3+} ions in the NaErF_4 core since Tm^{3+} has been previously proven to enhance the NIR-IIb emission of Er^{3+} through energy trapping.³⁰ Figure 1a presents the transmission electron microscopy (TEM) images of LnNPs, which are regular spherical and uniform with a mean particle diameter of 48 nm. High-resolution transmission electron microscopy (HRTEM) showed that the d spacing was 0.501 nm, corresponding to the (100) crystal plane (Figure 1b). High-angle annular dark-field scanning transmission electron microscopy (HAADF-STEM) images showed the core-multishell structured LnNPs (Figure 1c). The core diameter was 16 nm, the thickness of S1 (Y inert shell) was 6.15 nm, the thickness of S2 (YbTm active shell) was 4.9 nm, and the total thickness of S3 + S4 (Y and Gd inert shells) was 5.4 nm. X-ray diffraction (XRD) patterns indicated the pure β -phase of the core-multishell structural LnNPs, consistent with HRTEM observations (Figure 1f). Next, for theranostic application, as-obtained oleate-capped LnNPs were first treated with HCl to remove the oleic acid ligands and further modified using a polyallylamine solution. The Ce6 photosensitizers were attached to their surface to form the NIR-activated nanophotosensitizer, and the attachment was confirmed by Fourier transform infrared spectroscopy (FTIR) (Figure S1). A new characteristic peak at 1660 cm^{-1} indicated the chemical bond vibration resulting from the carboxylic and amino condensation reactions.

Subsequently, the as-obtained LnNP-Ce6 nanoparticles were functionalized with CaP: Mn coating according to a previously reported method.³¹ DOX was further loaded into the matrix of LnNP-Ce6@CaP: Mn, presenting pH-responsive Mn²⁺ ions and DOX release in a mildly acidic environment. The TEM image of the nanoplatform (Figure 1d) indicated a diameter of 56 nm and a thickness of 3 nm of the CaP layer. Elemental mapping of a single nanoplatform was first explored to obtain more details (Figure 1g). Energy-dispersive X-ray (EDX) spectroscopy further revealed the elements in the nanoplatform as Na, Ca, Mn, and rare-earth elements; Mn²⁺ was present at a concentration of 7.8 mol % (Figure 1h). The XRD patterns revealed the amorphous structure of CaP (Figure 1f). Previous studies have demonstrated that CaP nanoparticles are composed of smaller CaP particles, leading to pore structures on their matrix for drug loading. The drug-loading capacity of the nanoplatform was improved by increasing the thickness of the CaP layer by adjusting the ratio of isopropyl alcohol to water during the synthesis. TEM (Figure S2) revealed that the thickness of the CaP layer was 86 nm, and EDX, HAADF-STEM-EDS mapping, and linear scanning showed that the loading capacity of Mn²⁺ was significantly increased to 51.1 mol %.

The photoluminescence properties of LnNPs depended upon the excitation wavelength. Emission occurred in the red, green, and UV-blue regions upon excitation at 980 nm, because Er³⁺ in the core and Yb³⁺ in the shell were both excited (Figure 2a). In addition, the red upconversion luminescence

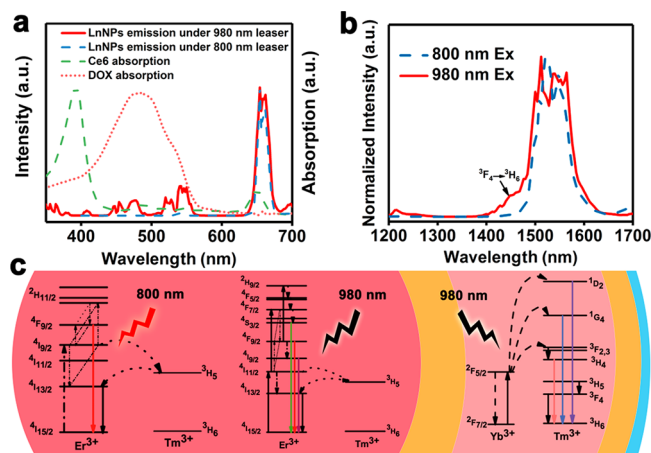


Figure 2. Spectral properties of LnNP-Ce6@CaP:Mn/DOX. (a) Upconversion emission spectra of LnNPs and absorption spectra of Ce6 and DOX. (b) Downshifting emission spectra of NaErF₄:0.5%Tm@ NaYF₄@ NaYbF₄:0.5%Tm@ NaYF₄@NaGdF₄ excited by 980 and 800 nm at 0.9 W/cm². (c) Schematic of the energy levels of LnNPs triggered by 980 and 800 nm, respectively.

(UCL) was almost 60-fold higher than the green emission at 540 nm because of the doping of a small amount of Tm³⁺ into the Er³⁺ lattice to effectively reduce the distribution at the high energy state of Er³⁺ through energy mediated by Tm³⁺. Energy transfer (ET) from Tm³⁺ to Er³⁺ occurred by back-energy transfer so that the NIR-IIb at 1525 nm and UCL at 655 nm of Er³⁺ have stronger emissions. Because of the inert shell, the 800 nm energy absorbed by Er³⁺ could hardly be transferred by Yb³⁺ ions to sensitize Tm³⁺. Importantly, no matter which excitation wavelength was used, the 1525 nm emission was always present, ensuring the subsequent imaging/diagnosis

application (Figure 2b). Furthermore, the full width at half-maximum of the 1525 nm emission peak under 980 nm excitation was wider than that of the 800 nm excitation peak due to the downshifting emission of Tm³⁺ ions at 1470 nm. Thus, the monochromaticity of 800 nm excitation was better than that of 980 nm excitation. The above-mentioned luminescence process and the corresponding energy level interpretation are shown in Figure 2c. Taken together, these photoswitchable LnNPs can be employed as an outstanding light transducer for deep tissue imaging and FRET-based phototherapy, i.e., NIR-IIb emission generated upon 808 nm excitation can be used for real-time optical imaging/diagnosis. Once the tumor site is accurately located by imaging, the excitation wavelength is switched to 980 nm, and the generated additional UV-blue light is used for PDT.

Furthermore, for achieving the 980 nm mediated PDT, the LnNPs-Ce6 nanophotosensitizer was prepared by coupling Ce6 with LnNPs. The optimal concentration of Ce6 on the surface of LnNPs was determined to be 4.8 μg/mL according to the results of our previous report.²¹ After that, the energy lifetime of the excitation states at 540 and 650 nm was measured. The lifetimes of both energy states were shortened, indicating ET between the LnNPs and the photosensitizer (Figure S3). The level of ROS production in the solution under different light excitations was investigated by employing 1,3-diphenylisobenzofuran (DPBF) as a ROS probe. Then, the ROS yield of the sample was measured by monitoring changes in the absorption intensity at 417 nm under 980 and 800 nm irradiation (Figure S4a). The photosensitizer produced abundant ROS upon 980 nm irradiation, but almost no ROS was detected upon 800 nm excitation because of the energy isolation layer, indicating negligible chances of phototoxicity during real-time optical imaging. The phototoxicity that may be caused by 800 nm excitation could be completely avoided by coupling another photosensitizer that does not absorb light at 650 nm or by increasing the thickness of the NaYF₄ middle shell to enlarge the FRET distance.

Cytotoxicity and Cell Uptake Behavior of the Nanoplatform *in Vitro*. First, the cellular uptake behavior of the nanoplatform in 4T1 breast cancer cells was analyzed using a fluorescence microscope. DAPI (4',6-diamidino-2-phenylindole) stains nucleic acids and exhibits blue fluorescence under 405 nm laser irradiation. The nanoplatform would emit red luminescence upon 980 nm excitation. As expected, on extending the incubation time from 3 to 12 h, the red luminescence from LnNPs increased gradually under the same excitation condition of 980 nm (Figure 3a), indicating that a greater amount of the nanoplatform was internalized by cells after incubation for 3 h. The transfection efficiency of the designed nanoplatform was quantified by measuring the UCL at 654 nm before and after incubating the cells with the nanoplatform. Given the stable spectral properties of LnNPs and the absence of payloads (DOX and Mn²⁺) that could otherwise have interfered with the analysis, the transfection efficiency was calculated as 61.25% (Figure S7). The bio-TEM results also confirmed the cellular uptake of the nanoplatform (Figure 3b). Part of the nanoplatform was located in the lysosome, indicating that the uptake of the nanoplatform occurred by endocytosis.

The methylthiazolyldiphenyl-tetrazolium bromide (MTT) assay was used to quantify the cytotoxicity of the nanoplatform at different concentrations against 4T1 cells (Figures S5b and 3d). The cytotoxicity of LnNP-Ce6@CaP/Mn²⁺ was first

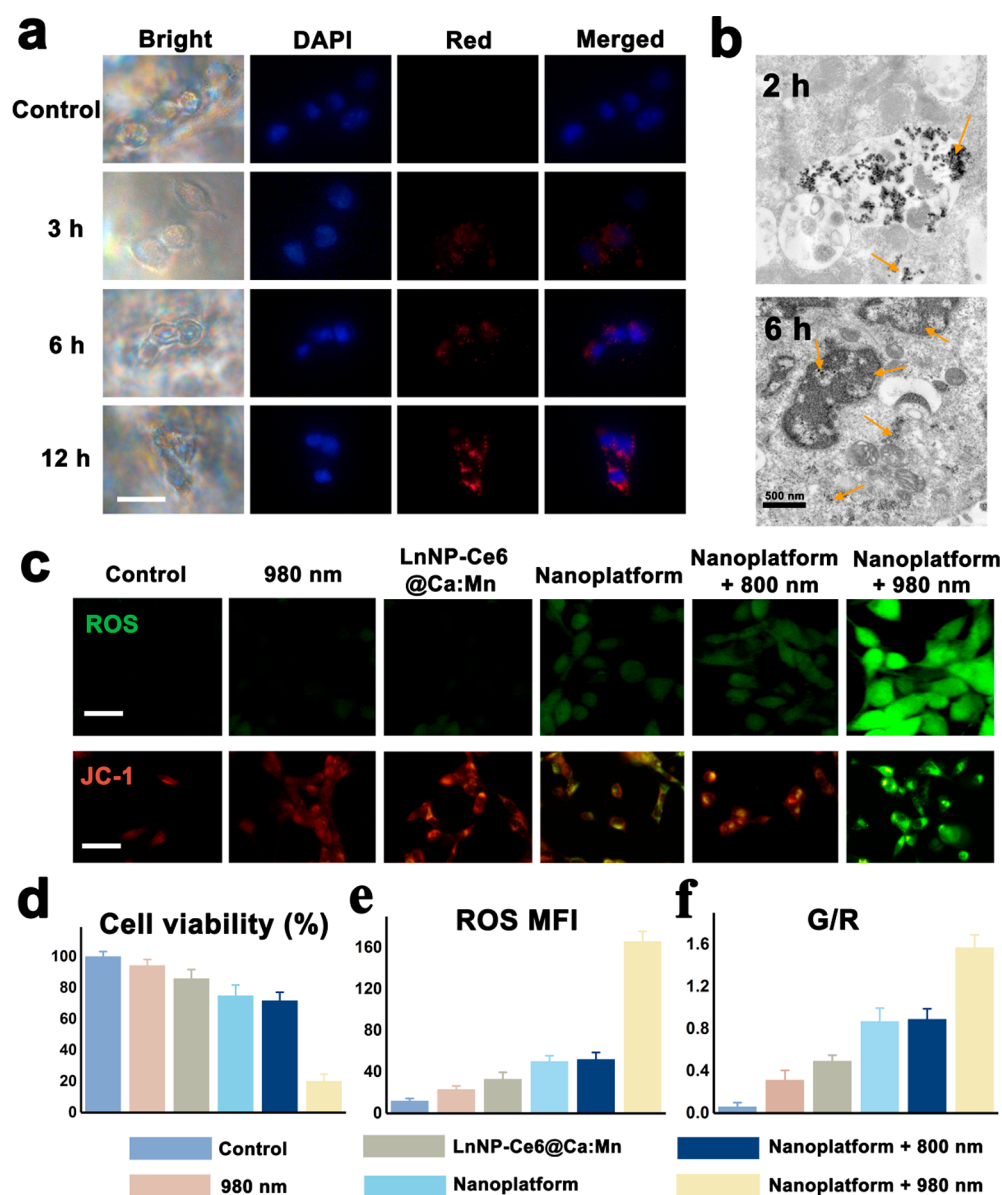


Figure 3. Mechanism evaluation of the nanoplatform-induced cell death by photodynamic/chemo-/immunotherapy. (a) Fluorescence photographs of 4T1 cells incubated with (1) PBS and (2) nanoplatform for different times. The blue and red fluorescence signals represent the cell nucleus and the nanoplatform, respectively. Scale bar: 50 μm . (b) The bio-TEM of 4T1 after incubating with the nanoplatform for 2 and 6 h. Scale bar: 500 nm. (c) Oxidative stress of 4T1 cells was observed in different treatment groups, using DCFH-DA as a ROS probe. Scale bar: 20 μm . JC-1 staining of cells in different treatment groups. Scale bar: 20 μm . (d) Cell viabilities of 4T1 cells with different treatment (PBS, 980 nm irradiation, LnNP-Ce6@Ca:Mn²⁺, nanoplatform, nanoplatform + 800 nm irradiation, and nanoplatform + 980 nm irradiation) versus the incubated sample. The fluorescence intensity of (e) DCFH-DA and (f) JC-1 was quantitatively analyzed using ImageJ. *, $P < 0.05$; **, $P < 0.01$; ***, $P < 0.001$, by Student's *t*-test.

evaluated in the dark (Figure S5a). When treated with the nanoplatform at concentrations below 48 $\mu\text{g}/\text{mL}$ for 24 h, the cell viability in the LnNP-Ce6@CaP/Mn²⁺ without irradiation group was more than 85%, indicating their good biocompatibility. The cytotoxicity of the nanoplatform was slightly increased due to DOX release. After exposure to 980 nm irradiation at 0.6 W/cm^2 , the nanoplatform exhibited considerably high phototoxicity, and the cell viability was only 19.6%, indicating the obvious effect of PDT. However, upon 800 nm laser irradiation, a negligible PDT effect was produced, ensuring that the real-time imaging did not cause any damage to the cells. Furthermore, the ROS production in 4T1 cells was visualized by using 2',7'-dichlorodihydrofluor-

escein diacetate (DCFH-DA) as a cell-permeable probe. Intracellular ¹O₂ could then be observed by confocal laser scanning microscopy (CLSM) after 980 nm PDT (Figure 3c). Compared with the control group, the green fluorescence intensity of cells treated with 980 nm irradiation, LnNP-Ce6@Ca:Mn²⁺, nanoplatform only, and nanoplatform + 800 nm irradiation increased to a certain extent, while the fluorescence intensity of the nanoplatform + 980 nm irradiation group increased significantly, indicating the strongest PDT effect. Figure 3e shows the quantitative analysis results of the ROS production in different experimental groups. The fluorescence intensity of ROS was 4 times higher in the group treated with LnNP-Ce6@CaP/Mn²⁺ loaded with DOX + 800 nm

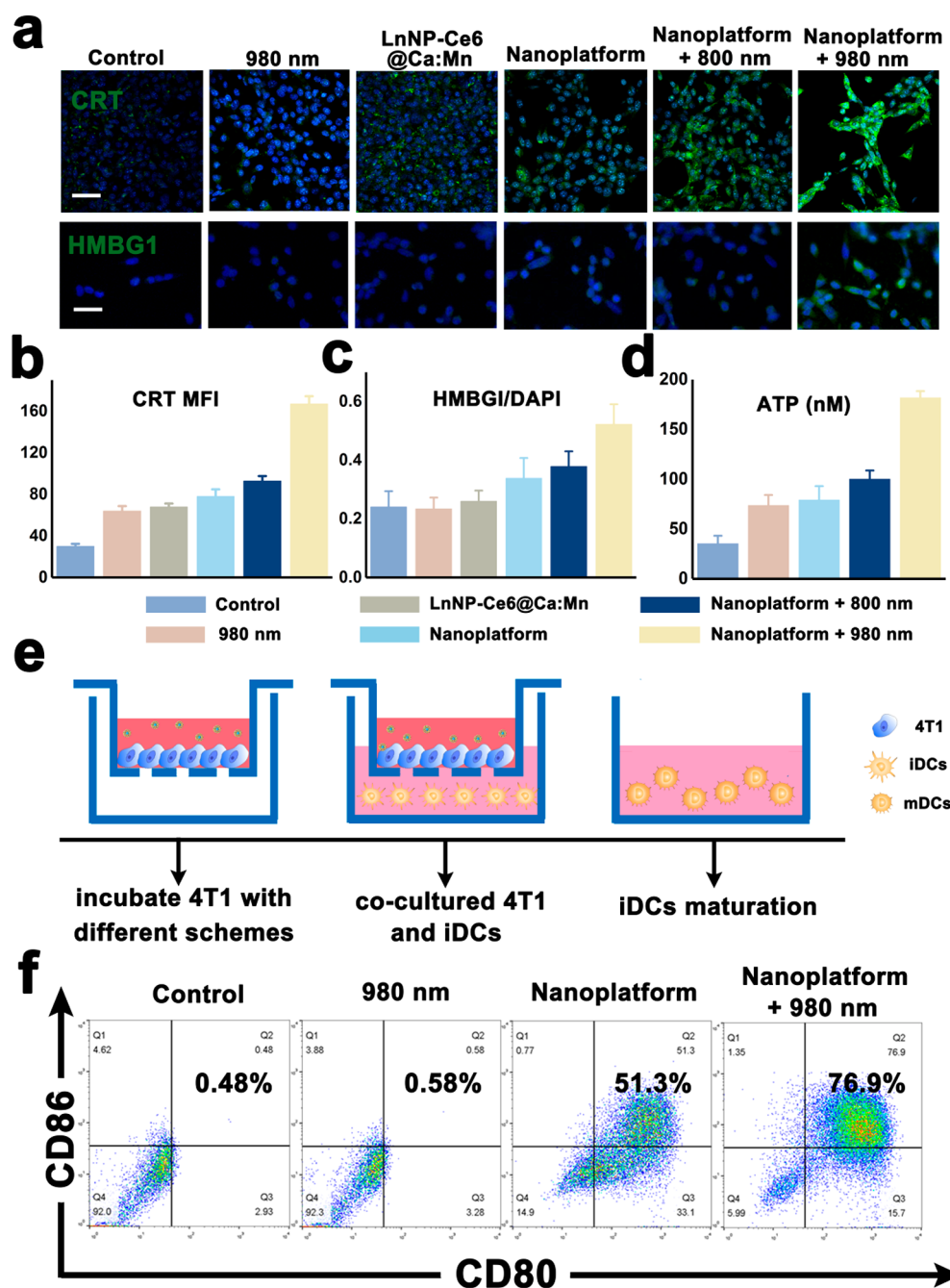


Figure 4. *In vitro* immune effect evaluation induced by the nanoplatform. (a) Expression of CRT and HMBG1 was observed by immunofluorescence staining. The green color indicates the CRT and HMBG1 flow from the endoplasmic reticulum. Scale bar: 100 μ m. The fluorescence intensities of (b) CRT and (c) HMBG1 were quantitatively analyzed using ImageJ. *, $P < 0.05$; **, $P < 0.01$; ***, $P < 0.001$, by Student's *t*-test. (d) Detection of the secretion of ATP by cells 4T1. (e) Schematic diagram of DCs maturation stimulated *in vitro*. (f) CD80 and CD86 detection by flow cytometry.

irradiation than that in the control group and 14 times higher in the nanoplatform + 980 nm irradiation group than that in the control group, indicating that the PDT effect of nanoplatform + 980 nm irradiation was stronger than that of the nanoplatform + 800 nm irradiation. The destructive effect of PDT on the mitochondrial membrane and apoptosis induction was studied next. A JC-1 assay was carried out to test the mitochondrial membrane potential after observation under a fluorescence microscope. The ratio of green (low potential, damage) to red (high potential, normal) fluorescence in the nanoplatform + 980 nm irradiation group reached

the highest value (1.5), which reflected mitochondrial dysfunction, and this was consistent with the trend seen in the cytotoxicity assay (Figure 3c,f).

Considering the important role of PDT in causing ICD, we investigated the CRT expression on 4T1 cells, a characteristic biomarker of ICD, which would migrate to the membrane surface from the endoplasmic reticulum under strong oxidative stress. The strongest fluorescence intensity was observed in the 980 nm triggered PDT group after 24 h of incubation, indicating the highest CRT migration (Figure 4a). The CRT fluorescence of 4T1 cells treated only with 980 nm irradiation

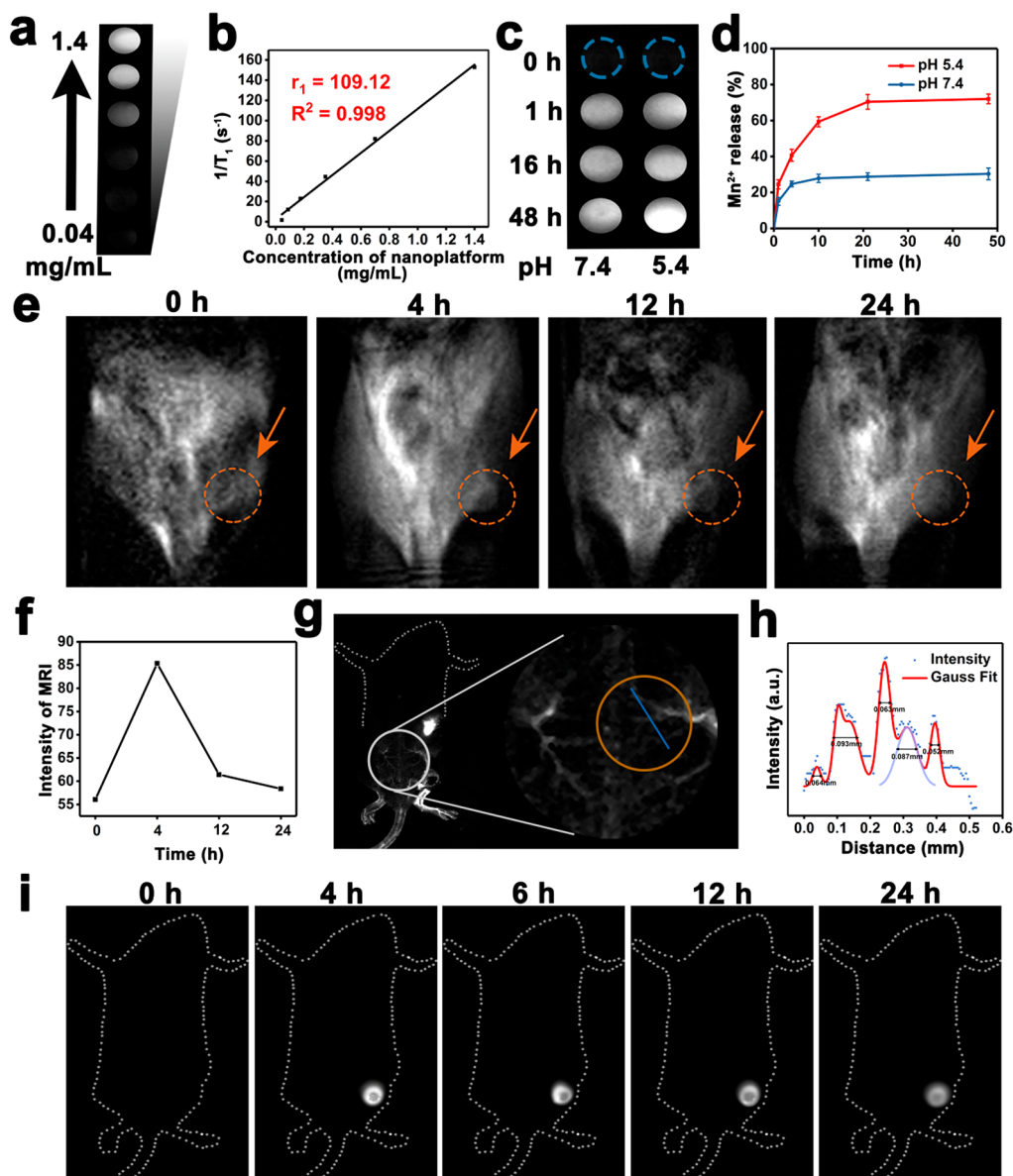


Figure 5. *In vivo* MR and NIR-IIb imaging. (a) T₁-weight MR images of different concentration nanoplateform. (b) Relaxation rates of the nanoplateform at different concentrations using a 1.2T MR scanner. (c) T₁-weight MR images of the nanoplateform against different pH conditions over time. (d) Release profiles determined by ICP. (e) T₁-weight MR images of tumor-bearing mice at different time points after intravenous (i.v.) injection of the nanoplateform. (f) Relative signal intensity in the tumor site. (g) NIR-IIb imaging of blood vessels, livers, and tumors upon 800 nm irradiation after i.v. injection. (h) Corresponding cross-sectional luminescence intensity curve and the Gaussian fitting curve along the blue line in panel (f). (i) Luminescence photos at the tumor site. Filter: 1500 nm long-pass.

was almost the same as that of the control group, and the fluorescence intensity was slightly increased after the introduction of the nanoplateform, indicating that the nanoplateform could induce an immune response in the cells (Figure 4b). However, the fluorescence intensity of CRT in the nanoplateform + 980 nm irradiation group was significantly enhanced (6-fold), indicating the prominent PDT-induced cellular immune response. Subsequently, the other two important biomarkers of ICD were also detected. In the presence of ATP, HMGB1 binds to Toll-like receptor 4 on the surface of dendritic cells (DCs), which promotes antigen presentation to T cells. After 12 h of incubation with the nanoplateform + 980 nm irradiation, the HMGB1 release increased 2-fold (Figure 4a,c). The amount of ATP secreted by the cells after PDT was 187 nmol L⁻¹, which was 5.8-fold

higher than that in control group (Figure 4d). Taken together, the results confirmed that treatment with the nanoplateform + 980 nm irradiation can induce ICD in tumor cells.

Due to the participation of HMDB1 and ATP in the DC-mediated immune response, we further tested the degree of maturation by quantifying mature dendritic cells (mDCs). DCs are special antigen-presenting cells, responsible for coordinating the immune response mediated by T cells. After phagocytosis of the antigen, iDCs process it into peptides. iDCs mature as they pass through lymph nodes and display peptide to T cells, which will differentiate into effector T cells and destroy tumor cells. In this experiment, 4T1 cells and bone marrow-derived iDCs were cocultured in a transwell system. After different treatments of 4T1 cells in the upper wells, iDCs were incubated in the lower wells for 24 h (Figure 4e). Then,

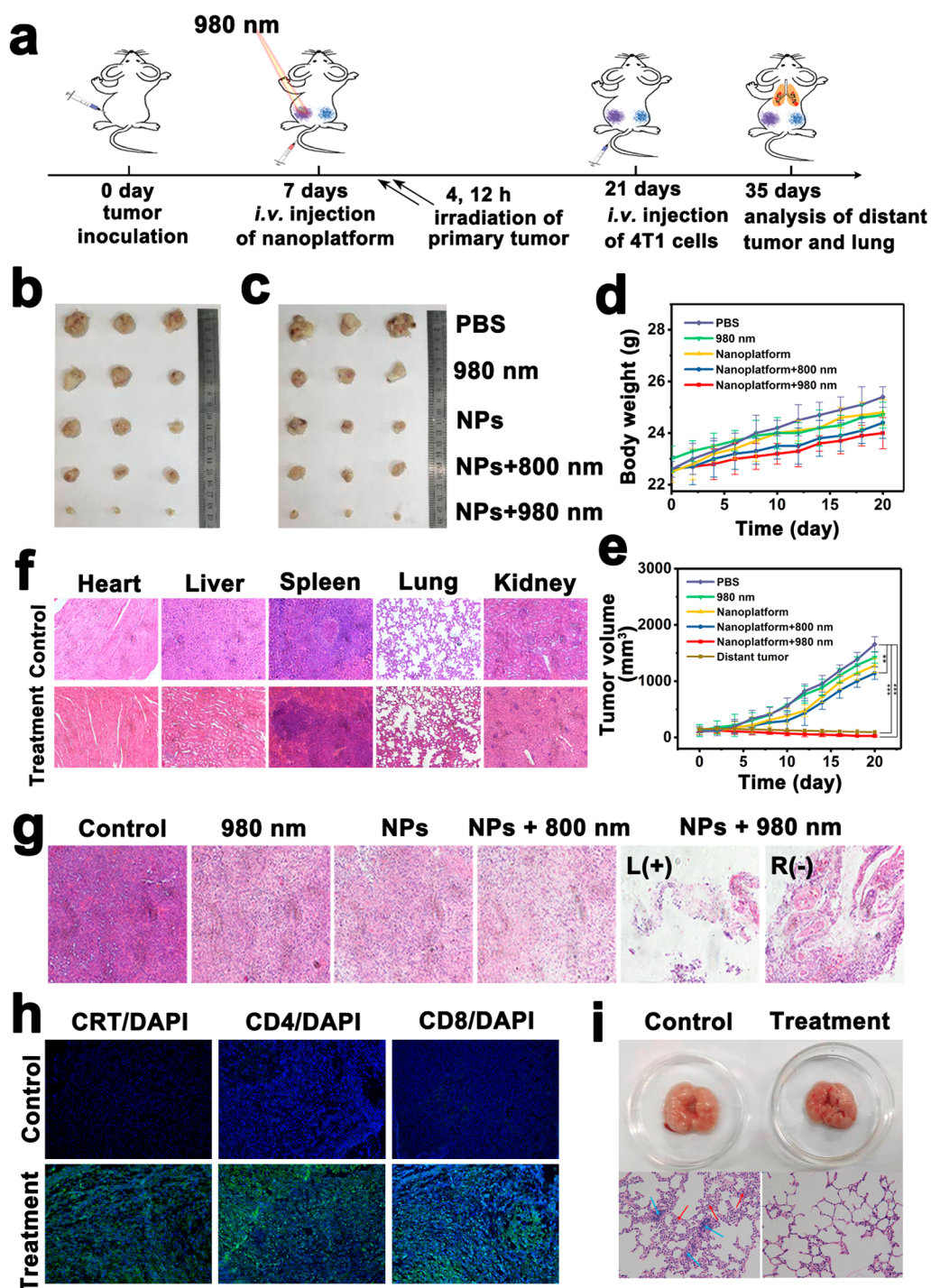


Figure 6. Nanoplatform-mediated inhibition of tumor growth in 4T1 tumor model. (a) Schedule diagram of the treatment. Photos of (b) primary tumors and (c) distant tumors. (d) Changes in the body weights of mice and (e) relative tumor volume in different groups. **, $P < 0.01$; ***, $P < 0.001$, by Student's t -test. (f) H&E staining images of major organs of mice in nanoplatform + 980 nm and control group. Scale bar: 150 μm . (g) H&E staining images of primary tumors in each group and distant tumor of nanoplatform + 980 nm group. Scale bar: 150 μm . (h) Immunofluorescence analysis of distant tumors in nanoplatform + 980 nm and control group. Scale bar: 100 μm . (i) Representative photographs of lung tissue and corresponding H&E staining images. Scale bar: 100 μm .

iDCs were collected to analyze the amounts of CD86 and CD80 proteins, which are biomarkers of mDCs, by flow cytometry. 4T1 cells incubated with the nanoplatform + 980 nm irradiation exhibited significant maturation of iDCs (76.9%) compared with that in the control group (0.48%) (Figure 4f). The maturation of the nanoplatform-only group

(without light irradiation) was 51.3%, which may be attributed to the immune response induced by DOX.

Evaluation of DOX and Mn^{2+} Release Profiles. The realization of pH-triggered TME-enhanced MRI and drug release for chemotherapy principally depends on the efficient release of Mn^{2+} and DOX from the matrix of nanoplatform. Thus, we analyzed their release profiles separately against

buffer solutions. At physiological pH (7.4, PBS solution), the nanoplatform exhibited prominent chemical stability, and the total Mn^{2+} leakage was as low as 30% after incubation for 48 h (Figure 5d) measured by inductively coupled plasma mass spectrometry (ICP-MS). Due to the low toxicity of Mn^{2+} , the toxicity of 30% Mn^{2+} leakage was almost negligible.³² In contrast, the nanoplatform samples exhibited a fast release pattern when incubated at pH 5.4, with a cumulative release percentage of 75% at 48 h, apparently indicating the sensitivity of the nanoplatform to an acidic environment (Figure 5d). The DOX release curve was determined by absorption intensity measurement, and the results were consistent with Mn^{2+} release behaviors. Specifically, after 24 h of incubation with PBS solution, the leakage of DOX was limited ($\sim 30\%$), while after 24 h of incubation in an acidic environment (pH 5.4), it increased to over 80% in a burst-release manner (Figure S6a). Furthermore, the color reaction between Mn^{2+} and NaBiO_3 also confirmed the release profile of Mn^{2+} in the various incubation solutions (Figure S6b). Afterward, the composite nanostructure after incubation was studied by SEM, and severe degradation of the CaP:Mn/DOX structure was observed at pH 5.4 (Figure S6d). SEM images showed that CaP:Mn coating was partially dissolved after incubation in pH 7.4 buffer for 48 h (Figure S6c). The determination of the concentrations of Ca^{2+} and Mn^{2+} ions by EDX (Figure S6e,f) also confirmed that the nanostructure accelerated the decomposition at pH 5.4. Furthermore, intracellular degradation of the nanoplatform was observed by bio-TEM analysis after coculture with 4T1 cells for 2 and 6 h (Figure 3b). Compared to 2 h of incubation, the reduced size and morphology of the nanoplatform at 6 h suggests the decomposition of CaP coating, which also indicates the release of Mn^{2+} and DOX within the cells.

In Vivo MR and NIR-IIb Luminescence Imaging Studies. Both Mn^{2+} and Gd^{3+} are paramagnetic which can be carried out as excellent contrast agents for T_1 -weighted MRI. The T_1 signal intensity was directly proportional to the concentration of the nanoplatform *in vitro* (Figure 5a), and the relaxation rate reached $109.12 \text{ s}^{-1} \text{ mg}^{-1}/\text{mL}^{-1}$ (Figure 5b). The MRI effect of the sample released *in vitro* at pH 7.4 and 5.4 at different time points is shown in Figure 5c. With time, the MRI signal was gradually enhanced and became significantly stronger than that at 0 h, because the surface modification of LnNPs hindered the interaction between water and Gd^{3+} . The concentrations of free Mn^{2+} and exposed Gd^{3+} increased after CaP decomposition in an acidic TME. Longitudinal comparison also showed a stronger signal at pH 5.4, which was consistent with the results of ICP-MS (Figure 5d). Furthermore, MRI signals were also tested at multiple time points in mice. The MRI signal at the tumor area gradually strengthened over time (Figure 5e). The T_1 -MR signal intensity increased to the maximum at 4 h postinjection (Figure 5f), i.e., the enrichment of nanoplatforms reached the maximum, indicating that it is the optimal treatment timing. The above results indicated that this nanoplatform can accumulate in the tumor region, facilitating preliminary tumor identification.

After identifying the initial location of the tumor by MRI, NIR-IIb imaging was carried out to accurately locate the tumor. Almost no luminescence signal was detected at the tumor site because of the low self-luminescence background radiation in the NIR-IIb window, while blood vessel, liver, and tumor tissues could be observed after intravenous injection (Figure 5g). The yellow circle shows an enlarged part of the

blood vessel. The fluorescence intensity of the cross section of the blue line was analyzed by Gauss fitting (Figure 5h). The narrowest blood vessel in the back of the mouse was $52 \mu\text{m}$ in diameter. Figure 5i shows the NIR-IIb imaging results at the tumor site over time. A 4 h after injection, the nanoplatforms were significantly enriched at the tumor site. Then, the luminous signals began to decrease after 6 h. The fluorescence signal could still be detected 24 h after injection; furthermore, the attenuation of the fluorescence with time was consistent with the MRI signal. Taken together, the *in vivo* imaging results suggest that the nanoplatform can act as an excellent NIR-IIb imaging probe.

In Vivo Antitumor Effect. Given the superior antitumor effect *in vitro*, the antitumor effect of the nanoplatform was investigated *in vivo* (Figure 6a). First, the pharmacokinetics of the nanoplatform was studied. The nanoplatform was injected intravenously into tumor-bearing mice, and the major organs and tumors of mice were collected at different times to determine the content of Er by ICP-MS. The nanoplatform accumulated at the tumor site; the concentration reached the maximum within 4 h and gradually decreased (Figure S8). The nanoplatform was also gradually metabolized from other major organs within 48 h.

Next, tumor-bearing mice were randomly divided into five groups and provided various treatments (control, 980 nm irradiation, nanoplatform, nanoplatform + 800 nm irradiation, and nanoplatform + 980 nm irradiation). The body weights of the mice showed no significant fluctuations over 20 days (Figure 6d), indicating little biotoxicity of the nanoplatform in mice. The photographs of tumor-bearing mice before and after treatment are shown in Figure S9. The primary and distant tumors of mice were collected after treatment (Figure 6b,c, respectively). The tumor volume changed significantly (Figure 6e) in the group treated with the nanoplatform + 980 nm irradiation ($0.6 \text{ W}/\text{cm}^2$), and it was the most effective among all five treatment groups, demonstrating an excellent synergistic therapeutic effect. By contrast, the tumor volume change in the nanoplatform + 800 nm irradiation ($0.6 \text{ W}/\text{cm}^2$) group was not obvious, indicating that 800 nm laser irradiation did not produce the PDT effect, consistent with the *in vitro* results. The tumors treated only with 980 nm irradiation or PBS also showed no significant inhibition, suggesting that irradiation and PBS had no therapeutic effect on tumors. Furthermore, the major organs (Figure 6f), primary tumor, and distant tumor (Figure 6g) were extracted and sectioned for staining with hematoxylin and eosin (H&E). The tumor cells in the 980 nm irradiation group were closely arranged, similar to the cells in the control group. The tumor cells in the nanoplatform group were slightly loosened due to the release of DOX at the tumor site. The primary tumor and distant tumor cells in the nanoplatform + 980 nm irradiation group exhibited extensively died, indicating the excellent therapeutic ability coupled with the ICD effect. Additionally, no noticeable histological damage or inflammation was observed in the main organs (heart, liver, spleen, lung, and kidney) of the treated mice.

Considering the easy metastasis of 4T1 tumor cells, we preliminarily studied the antitumor immune function of the nanoplatform. After recognizing the peptides processed by mature DCs, T cells in lymph nodes will differentiate into effector T cells, i.e., CD8^+ cytotoxic T cells and CD4^+ helper T cells. Immunofluorescence staining was carried out on the distant tumors of the nanoplatform + 980 nm irradiation and

PBS groups, and it was found that the numbers of CRT, CD8⁺ T cells, and CD4⁺ T cells in the treatment group were significantly increased (Figure 6h), indicating that the therapy consisting of nanoplatform + 980 nm irradiation can cause an antitumor immune response. After 21 days of treatment, 4T1 cells were intravenously injected, and the mice were euthanized 35 days later to observe pulmonary lesions. Lung metastases in the treatment group were less severe than those in the control group due to the autoimmune response (Figure 6i). Several lumps were observed in the control group; furthermore, the H&E staining images indicated vascularized tumor thrombus in the lung (blue arrows), and tumor cells infiltrated the pulmonary septum (red arrows). In the treatment group, healthy lungs with normal alveolar structure could be seen in the H&E staining images of the lung, indicating an obvious ICD response to 4T1 cells after treatment with nanoplatform + 980 nm irradiation. In short, the nanoplatform has superior biological safety and potent tumor therapeutic effect *in vivo*.

CONCLUSION

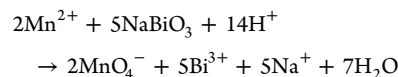
We established a dual-modal image-guided multifunctional theranostic nanoplatform for tumor therapy that combines diagnosis, therapeutics, and immunity. Tumor-targeted imaging and therapy are achieved by using pH-sensitive CaPs-capped photoswitched LnNP-Ce6 nanophotosensitizers as Mn²⁺/DOX carriers. Importantly, after the nanoplatform accumulated at the tumor site, the decomposition of CaP in the mildly acidic TME led to the release of Mn²⁺/DOX, which boosted their relaxation. Thus, the enhanced T₁-MRI allowed the preliminary identification of the tumor. Meanwhile, NIR-IIb emission of the nanoplatform stimulated by 800 nm light achieved accurate tumor location. Then, PDT was simulated by 980 nm irradiation along with guidance from the spatial high-resolution NIR-IIb imaging. Importantly, PDT combined with chemotherapy induced a potent ICD effect, thereby activating the antitumor immune response. As a result, effective inhibition of primary and distant tumor growth, as well as lung metastasis was achieved by the multifunctional nanoplatform. Consequently, it provides a potential strategy for dual-modal image-guided PDT/chemotherapy through direct tumoricidal effects and induction of ICD with immune response activation.

EXPERIMENTAL SECTION

Materials. Erbium(III) acetate hydrate (>99.9%), thulium(III) acetate hydrate (>99.9%), Ln₂O₃ (Ln: Y, Yb, and Tm > 99%), oleic acid (OA, 90%), 1-octadecene (ODE, 90%), sodium oleate (>99%), sodium trifluoroacetate (98%), trifluoroacetic acid (99%), Ca(OH)₂, Na₂HPO₄, MnCl₂, Chlorin e6 (Ce6), PAAm (Poly allylamine solution, 20 wt %), MTT, and 1,3-diphenylisobenzofuran (DPBF) were purchased from Sigma-Aldrich (St. Louis, MO, USA). Ammonium fluoride (>98%), methanol, acetone, ethanol, cyclohexane, isopropanol (IPA), and *N,N*-dimethylformamide (DMF) were purchased from GFS Chemical. All materials were used without further purification. DCFH-DA ROS Assay Kit, Mitochondrial Membrane Potential Assay Kit with JC-1, Calreticulin Rabbit Monoclonal Antibody, HMBG1 Rabbit Monoclonal Antibody, Alexa Fluor 488-labeled Goat Anti-Rabbit IgG, ATP Assay Kit, CD4 Rabbit Monoclonal Antibody, and CD8 Rabbit Monoclonal Antibody was purchased from Beyotime Biotechnology Co., Ltd. (Shanghai, China). Doxorubicin was purchased from Solarbio (Beijing, China). CD80 Monoclonal Antibody FITC and CD86 Monoclonal Antibody PE were purchased from BioLegend (USA).

pH-Triggered Release of Mn²⁺ Ions from the Nanoplatform. First, 8 mL of the nanoplatform solution was added to a dialysis bag (MW cutoff = 3500) and placed in a beaker containing 20 mL of

buffer solutions with different pH values (pH 5.4 and 7.4) under vigorous stirring. Then, 1 mL of the solution in the beaker was removed to detect the concentration of Mn²⁺ by ICP-MS at different time points. Furthermore, the release of Mn²⁺ ions can be visualized by the color reaction. Briefly, 0.5 mL of solutions were taken from the beaker and added to 4 mg/mL NaBiO₃ solution (5 mol/L, HNO₃) to observe the color change from colorless to violet. The detection principle is that NaBiO₃ and Mn²⁺ can form MnO₄⁻ under acidic conditions, resulting in an absorption peak of MnO₄⁻ at 530 nm by the following reaction.



DOX Release Rate Analysis. The as-obtained nanoplatform solution (4 mL) was centrifuged and redispersed into 4 mL of buffer solutions with different pH values (pH 5.4 and 7.4). Then, 200 μL of the incubation liquid was centrifuged to remove the nanoplatform, and the DOX absorption of the supernatant value at 492 nm was detected at regular intervals. After each measurement, 200 μL of the supernatant and the nanoplatform was poured back into the incubation solution.

MTT Assay for Evaluating the Cytotoxicity of the Nanoplatform. The cytotoxicity of the nanoplatform was evaluated using 4T1 tumor cells, which were cultured in RPMI medium 1640 containing 10% fetal bovine serum in 5% CO₂ at 37 °C. The cells were seeded on 96-well plates, then incubated overnight. After adherent growth, 10 μL of the nanoplatform at different concentrations were added to the wells and further incubated for 12 h. The three groups were treated with no irradiation, 980 nm irradiation, and 800 nm irradiation. After another 12 h of incubation, 10 μL of MTT solution (5 mg/mL) was added to each well. After 4 h of incubation, the above solution was replaced with 100 μL of DMSO. Finally, the absorbance at 492 nm was detected using a microplate reader (BioTek808, USA).

Cellular Uptake Behaviors of the Nanoplatform via UCL Imaging and Bio-TEM. 4T1 cells (10⁵ cells per dish) were cultured in glass-bottomed dishes for 12 h to obtain monolayer cells, and incubated with the samples for 3, 6, and 12 h. Then, DAPI staining was carried out, and to eliminate the residual substances clearly, the cells were washed three times with PBS. UCL imaging was detected on a Nikon C2si microscope unit equipped with a 980 and 800 nm continuous wave laser.

Monolayer 4T1 cells were seeded in a 6-well plate, and the nanoplatform (0.1 mg mL⁻¹, 100 μL) was added to the culture medium. After incubating for 2 and 6 h, the cells were washed, collected, and finally fixed with 2% glutaraldehyde and observed by bio-TEM.

Detection of the Transfection Efficiency of the Nanoplatform. 4T1 cells were incubated in a 6-well plate at a density of 2 × 10⁵ for 24 h, and then the nanoplatform (100 μL, 0.1 mg mL⁻¹) was added into the culture medium. After incubation for 1, 4, and 10 h, the cells were washed with PBS. Then, the cells were lysed and dispersed in 1 mL of water to record the emission spectrum of the nanoplatform upon 980 nm excitation. The transfection efficiency was calculated according to the integral area at 650 nm as follows: $E\% = I_{\text{uptake}}/I_0 \times 100\%$ or $E\% = (1 - I_{\text{medium}}/I_0) \times 100\%$.

In Vitro Detection of ROS Production. The 4T1 cells were incubated in a glass-bottomed dish at a density of 2 × 10⁵ cells/dish for 24 h and were subjected to different treatments: (1) PBS, (2) 980 nm irradiation, (3) LnNP-Ce6@Ca:Mn²⁺, (4) nanoplatform, (5) nanoplatform + 800 nm irradiation (0.6 W/cm²), and (6) nanoplatform + 980 nm irradiation (0.6 W/cm²). After 20 h, the cells were washed thrice with PBS, and DCFH-DA was then added to incubate for 20 min. After that, the cells were washed, and the green luminescence was recorded by CLSM.

Detection of Mitochondrial Membrane Potential. The 4T1 cells were incubated in a glass-bottom dish at a density of 2 × 10⁵ cells/dish for 24 h, and then the cells were subjected to different treatments: (1) PBS, (2) 980 nm irradiation, (3) LnNP-Ce6@

Ca:Mn²⁺, (4) nanoplatform, (5) nanoplatform + 800 nm laser, and (6) nanoplatform + 980 nm laser. After 20 h, the culture medium was replaced, and the cells were incubated with JC-1 (5 μg/mL) at 37 °C for 20 min. Then, the cells were washed three times with PBS. After that, the cells were imaged by CLSM.

Detection of CRT and HMBG1 Expression. The 4T1 cells were seeded in a glass-bottom dish for 24 h, then the cells were subjected to different treatments: (1) PBS, (2) 980 nm irradiation, (3) LnNP-Ce6@Ca:Mn²⁺, (4) nanoplatform, (5) nanoplatform + 800 nm laser, and (6) nanoplatform + 980 nm laser. After 20 h, the cells were washed with PBS and fixed with 4% paraformaldehyde for 15 min at 37 °C. Then, the cells were incubated with 0.3% Triton X-100 for 5 min at room temperature and washed. Subsequently, the cells were incubated with CRT rabbit monoclonal antibody at 37 °C for 1 h and 1% bovine serum albumin (BSA) for another 1 h at 37 °C, then incubated with Alexa Fluor 488-labeled secondary antibody for 1 h after washing thrice with PBS. Finally, the cell nuclei were stained with DAPI and observed by CLSM. The detection method of HMBG1 was similar to that of CRT.

Detection of ATP Secretion *in Vitro*. The 4T1 cells were seeded 6-well plates at a density of 2 × 10⁵ cells/well for 24 h, and then the cells were treated with different methods: (1) PBS, (2) 980 nm irradiation, (3) nanoplatform, (4) nanoplatform + 800 nm irradiation, and (5) nanoplatform + 980 nm irradiation. The cells were lysed and centrifuged after 20 h incubating. The content of ATP was detected according to the instruction of the ATP Assay Kit.

***In Vitro* Stimulation of DCs.** DC differentiation experiments were carried out using a 6-well transwell system with 0.4 μm polycarbonate porous membranes. First, bone marrow-derived DCs were extracted from 6–8 week old BALB/c female mice and then cultured for 7 days. Then, 1 × 10⁴ 4T1 cells were seeded into the upper well and treated with PBS, 980 nm irradiation, nanoplatform, and nanoplatform + 980 nm irradiation. The above-mentioned cultured DCs were seeded in the lower well and further cocultured for another 24 h. Finally, DCs were collected and stained with 3 μL of anti-CD86 PE (0.2 mg mL⁻¹) and 3 μL of anti-CD80 FITC (0.2 mg mL⁻¹). After 20 min, DCs were centrifuged, washed three times, and detected by flow cytometry.

MRI and NIR-IIb Imaging. First, T₁-weight MR images of the nanoplatform diluted 1, 2, 4, 6, 8, 10 times with PBS were carried out. T₁-weight MR images tests were obtained on a 1.2 T MRI scanner (Shanghai, China). Then, the relaxation rate of *r*₁ was determined through the curve fitting of 1/T₁ with the concentration of the nanoplatform. Finally, to observe the release of Mn²⁺ at different pH values, the nanoplatform was added to the dialysis bags and incubated in pH 5.4 and 7.4 buffer solutions for 48 h, respectively. The supernatant was sampled at different time points for MRI imaging.

All animal experiments were treated in line with the animal experiments ethical committee for care and use of research animals. Female BALB/c mice (6–8 weeks, body weight: ~20 g) were purchased from Vital River Company in Beijing. All animal experiments were observed in the Animal care and Use Committee of Northeastern University. For tumor-bearing studies, the xenograft tumor model was established by subcutaneously injecting 1 × 10⁶ 4T1 cells into the flanks of mice. When the inoculated tumor reached 50–100 cm³ in volume, the mice were intravenously injected the nanoplatform (0.2 mg/mL, 200 μL) and then anesthetized through intraperitoneal injection of 5% chloral hydrate (PBS, 100 μL). Afterward, the mice were imaged with an InGaAs camera (NIRvana-HS, Princeton Instruments, USA) (with 1500 nm long-pass filter) and a 1.2 T MRI scanner (Shanghai, China), respectively, at different time points (3, 6, 12, and 48 h).

Detection Pharmacokinetics of the Nanoplatform. Three tumor-bearing mice were euthanized at 4 h, 12 and 48 h respectively, after injecting intravenously the nanoplatform (0.2 mg mL⁻¹, 0.2 mL). The main organs and tumors were taken to measure the content of Er by ICP-MS.

Evaluation of Antitumor Efficacy *in Vivo*. For the combination antitumor therapy, tumor-bearing mice were randomly divided into five groups (*n* = 5) and treated with PBS (control group), 980 nm

irradiation, nanoplatform, nanoplatform + 800 nm irradiation, and nanoplatform + 980 nm irradiation. The mice were intravenously injected with the nanoplatform (0.2 mg mL⁻¹, 200 μL). After 4 and 12 h postinjection, the tumor site of each mouse in the irradiation groups was exposed to the corresponding laser for 15 min (980 or 800 nm, 0.6 W/cm²). The body weights and tumor volumes of mice were recorded every 2 days. Tumor volume (*V*) was determined by measuring the length (*L*) and width (*W*) and calculated as *V* = *L* × *W*²/2. After 14 days, half of the mice in each group were randomly selected for euthanasia. Then the tumors and major organs were harvested for subsequent analysis. The tissues were fixed with formalin and then paraffin-embedded. Furthermore, the paraffin-embedded tissues were sectioned and stained with H&E to determine tissue damage after observing under a microscope.

Evaluation of the Antitumor Immune Response. On day 14, the mice in the control and nanoplatform + 980 nm irradiation groups were intravenously injected with 2 × 10⁵ 4T1 cells per mouse to establish a lung metastatic breast cancer model. After 14 days, the mice were euthanized to collect the distant tumors for immunofluorescence staining. The tissues were fixed with formalin and dewatered twice with 30% sucrose solution for 24 h and then stored at -80 °C in OCT. The frozen tumor sections were treated with 0.1% Triton X-100 (PBS) for 45 min and incubated with CRT, CD4, and CD8 primary antibodies overnight at 4 °C, then incubated with 2% BSA for another 1 h. After PBS washing, the sections were incubated with Alexa Fluor 488-labeled secondary antibody for 1 h at room temperature. After DAPI staining, the cells were observed by CLSM. The lungs of the corresponding groups of mice were collected, fixed with paraformaldehyde, embedded in paraffin, and finally observed by CLSM after H&E staining.

ASSOCIATED CONTENT

Supporting Information

The Supporting Information is available free of charge at <https://pubs.acs.org/doi/10.1021/acsnano.1c09635>.

Synthesis of the nanoplatform; infrared spectra of LnNPs; TEM, EDX, and HAADF-STEM-EDS mapping; linear scanning image of the optimized nanoplatform; lifetime curve of LnNPs; *in vitro* evaluation of ROS production; *in vitro* cytotoxicity of LnNP-Ce6@CaP:Mn; drug release evaluation of nanoplatform in different pH environments; transfection efficiency test; pharmacokinetics of the nanoplatform; images of mice before and after different treatments (PDF)

AUTHOR INFORMATION

Corresponding Author

Yulei Chang – State Key Laboratory of Luminescence and Applications, Changchun Institute of Optics, Fine Mechanics and Physics, Chinese Academy of Sciences, Changchun 130033 Jilin, China; orcid.org/0000-0001-7223-1797; Email: yuleichang@ciomp.ac.cn

Authors

Haoran Chen – State Key Laboratory of Luminescence and Applications, Changchun Institute of Optics, Fine Mechanics and Physics, Chinese Academy of Sciences, Changchun 130033 Jilin, China; University of the Chinese Academy of Sciences, Beijing 100049, China

Fengxia Wu – Institute of Molecular Medicine, College of Life and Health Sciences, Northeastern University, Shenyang, Liaoning 110000, China

Xiaoyu Xie – State Key Laboratory of Luminescence and Applications, Changchun Institute of Optics, Fine Mechanics and Physics, Chinese Academy of Sciences, Changchun

130033 Jilin, China; University of the Chinese Academy of Sciences, Beijing 100049, China

Wang Wang – State Key Laboratory of Luminescence and Applications, Changchun Institute of Optics, Fine Mechanics and Physics, Chinese Academy of Sciences, Changchun 130033 Jilin, China; University of the Chinese Academy of Sciences, Beijing 100049, China

Qiqing Li – State Key Laboratory of Luminescence and Applications, Changchun Institute of Optics, Fine Mechanics and Physics, Chinese Academy of Sciences, Changchun 130033 Jilin, China

Langping Tu – State Key Laboratory of Luminescence and Applications, Changchun Institute of Optics, Fine Mechanics and Physics, Chinese Academy of Sciences, Changchun 130033 Jilin, China

Bin Li – State Key Laboratory of Luminescence and Applications, Changchun Institute of Optics, Fine Mechanics and Physics, Chinese Academy of Sciences, Changchun 130033 Jilin, China

Xiangui Kong – State Key Laboratory of Luminescence and Applications, Changchun Institute of Optics, Fine Mechanics and Physics, Chinese Academy of Sciences, Changchun 130033 Jilin, China

Complete contact information is available at:

<https://pubs.acs.org/10.1021/acsnano.1c09635>

Author Contributions

H.C. and Y.C. designed the research. H.C. and F.W. carried out the experiments. X.X. and W.W. carried out morphology characterization. H.C., F.W., and Y.C. wrote the manuscript. Q.L., L.T., X.K., and B.L. gave suggestions on the experiments and manuscript. All authors contributed to the discussion of the work.

Notes

The authors declare no competing financial interest.

ACKNOWLEDGMENTS

We gratefully acknowledge the financial support provided by the National Natural Science Foundation of China (62075217, 51772122, 11874354, 11874355, 61575194, and 22172154), Project of Science and Technology Agency, Jilin Province (20210101148JC), and the State Key Laboratory of Luminescence and Applications (SKLA-2019-02, SKLA-2020-09).

REFERENCES

- (1) Han, K.; Wang, S. B.; Lei, Q.; Zhu, J. Y.; Zhang, X. Z. Ratiometric Biosensor for Aggregation-Induced Emission-Guided Precise Photodynamic Therapy. *ACS Nano* **2015**, *9* (10), 10268–77.
- (2) Huang, P.; Lin, J.; Wang, S.; Zhou, Z.; Li, Z.; Wang, Z.; Zhang, C.; Yue, X.; Niu, G.; Yang, M.; Cui, D.; Chen, X. Photosensitizer-Conjugated Silica-Coated Gold Nanoclusters for Fluorescence Imaging-Guided Photodynamic Therapy. *Biomaterials* **2013**, *34* (19), 4643–4654.
- (3) Chen, Q.; Liu, L.; Lu, Y.; Chen, X.; Zhang, Y.; Zhou, W.; Guo, Q.; Li, C.; Zhang, Y.; Zhang, Y.; Liang, D.; Sun, T.; Jiang, C. Tumor Microenvironment-Triggered Aggregated Magnetic Nanoparticles for Reinforced Image-Guided Immunogenic Chemotherapy. *Adv. Sci. (Weinh)* **2019**, *6* (6), 1802134.
- (4) Obeid, M.; Tesniere, A.; Ghiringhelli, F.; Fimia, G. M.; Apetoh, L.; Perfettini, J. L.; Castedo, M.; Mignot, G.; Panaretakis, T.; Casares, N.; Metivier, D.; Larochette, N.; van Endert, P.; Ciccosanti, F.; Piacentini, M.; Zitvogel, L.; Kroemer, G. Calreticulin Exposure

Dictates the Immunogenicity of Cancer Cell Death. *Nat. Med.* **2007**, *13* (1), 54–61.

(5) Martins, I.; Wang, Y.; Michaud, M.; Ma, Y.; Sukkurwala, A. Q.; Shen, S.; Kepp, O.; Metivier, D.; Galluzzi, L.; Perfettini, J. L.; Zitvogel, L.; Kroemer, G. Molecular Mechanisms of ATP Secretion during Immunogenic Cell Death. *Cell Death Differ.* **2014**, *21* (1), 79–91.

(6) Apetoh, L.; Ghiringhelli, F.; Tesniere, A.; Criollo, A.; Ortiz, C.; Lidereau, R.; Mariette, C.; Chaput, N.; Mira, J. P.; Delaloge, S.; Andre, F.; Tursz, T.; Kroemer, G.; Zitvogel, L. The Interaction between HMGB1 and TLR4 Dictates the Outcome of Anticancer Chemotherapy and Radiotherapy. *Immunol. Rev.* **2007**, *220*, 47–59.

(7) Wilson, B. C.; Jeeves, W. P.; Lowe, D. M. *In Vivo* and Post Mortem Measurements of the Attenuation Spectra of Light in Mammalian Tissues. *Photochem. Photobiol.* **1985**, *42* (2), 153–62.

(8) Zuo, J.; Tu, L.; Li, Q.; Feng, Y.; Que, I.; Zhang, Y.; Liu, X.; Xue, B.; Cruz, L. J.; Chang, Y.; Zhang, H.; Kong, X. Near Infrared Light Sensitive Ultraviolet-Blue Nanophotoswitch for Imaging-Guided “Off-On” Therapy. *ACS Nano* **2018**, *12* (4), 3217–3225.

(9) Tang, M.; Zhu, X.; Zhang, Y.; Zhang, Z.; Zhang, Z.; Mei, Q.; Zhang, J.; Wu, M.; Liu, J.; Zhang, Y. Near-Infrared Excited Orthogonal Emissive Upconversion Nanoparticles for Imaging-Guided On-Demand Therapy. *ACS Nano* **2019**, *13* (9), 10405–10418.

(10) Zhong, Y.; Ma, Z.; Wang, F.; Wang, X.; Yang, Y.; Liu, Y.; Zhao, X.; Li, J.; Du, H.; Zhang, M.; Cui, Q.; Zhu, S.; Sun, Q.; Wan, H.; Tian, Y.; Liu, Q.; Wang, W.; Garcia, K. C.; Dai, H. *In Vivo* Molecular Imaging for Immunotherapy Using Ultra-Bright Near-Infrared-IIB Rare-Earth Nanoparticles. *Nat. Biotechnol.* **2019**, *37* (11), 1322–1331.

(11) Wang, H.; Wang, Z.; Tu, Y.; Li, Y.; Xu, T.; Yang, M.; Wang, P.; Gu, Y. Homotypic Targeting Upconversion Nano-Reactor for Cascade Cancer Starvation and Deep-Tissue Phototherapy. *Biomaterials* **2020**, *235*, 119765.

(12) Hou, Z.; Deng, K.; Li, C.; Deng, X.; Lian, H.; Cheng, Z.; Jin, D.; Lin, J. 808 nm Light-Triggered and Hyaluronic Acid-Targeted Dual-Photosensitizers Nanoplatfrom by Fully Utilizing Nd³⁺-Sensitized Upconversion Emission with Enhanced Anti-Tumor Efficacy. *Biomaterials* **2016**, *101*, 32–46.

(13) Chen, G.; Qiu, H.; Prasad, P. N.; Chen, X. Upconversion Nanoparticles: Design, Nanochemistry, and Applications in Theranostics. *Chem. Rev.* **2014**, *114* (10), 5161–214.

(14) Fan, W.; Huang, P.; Chen, X. Overcoming the Achilles’ Heel of Photodynamic Therapy. *Chem. Soc. Rev.* **2016**, *45* (23), 6488–6519.

(15) Jia, T.; Wang, Z.; Sun, Q.; Dong, S.; Xu, J.; Zhang, F.; Feng, L.; He, F.; Yang, D.; Yang, P.; Lin, J. Intelligent Fe-Mn Layered Double Hydroxides Nanosheets Anchored with Upconversion Nanoparticles for Oxygen-Elevated Synergetic Therapy and Bioimaging. *Small* **2020**, *16* (46), No. 2001343.

(16) Hou, Z.; Deng, K.; Wang, M.; Liu, Y.; Chang, M.; Huang, S.; Li, C.; Wei, Y.; Cheng, Z.; Han, G.; Al Kheraif, A. A.; Lin, J. Hydrogenated Titanium Oxide Decorated Upconversion Nanoparticles: Facile Laser Modified Synthesis and 808 nm Near-Infrared Light Triggered Phototherapy. *Chem. Mater.* **2019**, *31* (3), 774–784.

(17) Huang, H.; Huang, Y.; Chen, Y.; Luo, Z.; Zhang, Z.; Sun, R.; Wan, Z.; Sun, J.; Lu, B.; Zhang, L.; Hu, J.; Li, S. A Novel Immunochemotherapy Based On Targeting of Cyclooxygenase and Induction of Immunogenic Cell Death. *Biomaterials* **2021**, *270*, 120708.

(18) Hu, M.; Zhang, J.; Kong, L.; Yu, Y.; Hu, Q.; Yang, T.; Wang, Y.; Tu, K.; Qiao, Q.; Qin, X.; Zhang, Z. Immunogenic Hybrid Nanovesicles of Liposomes and Tumor-Derived Nanovesicles for Cancer Immunotherapy. *ACS Nano* **2021**, *15* (2), 3123–3138.

(19) Wang, D.; Xue, B.; Ohulchanskyy, T. Y.; Liu, Y.; Yakovliev, A.; Ziniuk, R.; Xu, M.; Song, J.; Qu, J.; Yuan, Z. Inhibiting Tumor Oxygen Metabolism and Simultaneously Generating Oxygen by Intelligent Upconversion Nanotherapeutics for Enhanced Photodynamic Therapy. *Biomaterials* **2020**, *251*, 120088.

(20) Xu, J.; Shi, R.; Chen, G.; Dong, S.; Yang, P.; Zhang, Z.; Niu, N.; Gai, S.; He, F.; Fu, Y.; Lin, J. All-in-One Theranostic Nanomedicine with Ultrabright Second Near-Infrared Emission for Tumor-

Modulated Bioimaging and Chemodynamic/Photodynamic Therapy. *ACS Nano* **2020**, *14* (8), 9613–9625.

(21) Li, Q.; Li, X.; Zhang, L.; Zuo, J.; Zhang, Y.; Liu, X.; Tu, L.; Xue, B.; Chang, Y.; Kong, X. An 800 nm Driven $\text{NaErF}_4@/\text{NaLuF}_4$ Upconversion Platform for Multimodality Imaging and Photodynamic Therapy. *Nanoscale* **2018**, *10* (26), 12356–12363.

(22) Skripka, A.; Karabanovas, V.; Jarockyte, G.; Marin, R.; Tam, V.; Cerruti, M.; Rotomskis, R.; Vetrone, F. Decoupling Theranostics with Rare Earth Doped Nanoparticles. *Adv. Funct. Mater.* **2019**, *29* (12), 1970073.

(23) Liu, L.; Wang, S.; Zhao, B.; Pei, P.; Fan, Y.; Li, X.; Zhang, F. Er^{3+} Sensitized 1530 to 1180 nm Second Near-Infrared Window Upconversion Nanocrystals for *in Vivo* Biosensing. *Angew. Chem., Int. Ed.* **2018**, *57* (25), 7518–7522.

(24) Zhong, Y.; Ma, Z.; Zhu, S.; Yue, J.; Zhang, M.; Antaris, A. L.; Yuan, J.; Cui, R.; Wan, H.; Zhou, Y.; et al. Boosting the Down-Shifting Luminescence of Rare-Earth Nanocrystals for Biological Imaging beyond 1500 nm. *Nat. Commun.* **2017**, *8*, 737.

(25) Zhang, H.; Fan, Y.; Pei, P.; Sun, C.; Lu, L.; Zhang, F. Tm^{3+} -Sensitized NIR-II Fluorescent Nanocrystals for *in Vivo* Information Storage and Decoding. *Angew. Chem., Int. Ed.* **2019**, *58* (30), 10153–10157.

(26) Lin, H.; Lin, Z.; Zheng, K.; Wang, C.; Lin, L.; Chen, J.; Song, J. Near-Infrared-II Nanomaterials for Fluorescence Imaging and Photodynamic Therapy. *Adv. Opt. Mater.* **2021**, *9*, 2002177.

(27) Li, F.; Li, T.; Zhi, D.; Xu, P.; Wang, W.; Hu, Y.; Zhang, Y.; Wang, S.; Matula Thomas, J.; Beauchamp Norman, J.; Ding, W.; Yan, L.; Qiu, B. Novel Ultrasmall Multifunctional Nanodots for Dual-Modal MR/NIR-II Imaging-Guided Photothermal Therapy. *Biomaterials* **2020**, *256*, 120219.

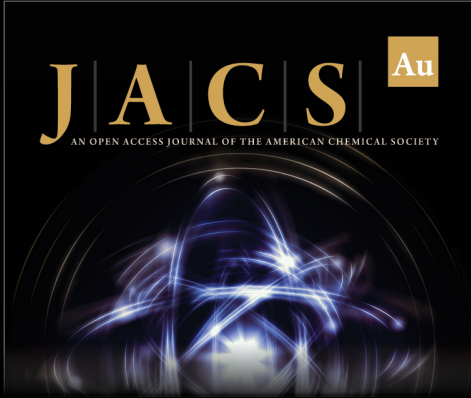
(28) Zheng, Z.; Jia, Z.; Qu, C.; Dai, R.; Qin, Y.; Rong, S.; Liu, Y.; Cheng, Z.; Zhang, R. Biodegradable Silica-Based Nanotheranostics for Precise MRI/NIR-II Fluorescence Imaging and Self-Reinforcing Antitumor Therapy. *Small* **2021**, *17* (10), No. 2006508.

(29) Yi, Z.; Luo, Z.; Barth, N. D.; Meng, X.; Liu, H.; Bu, W.; All, A.; Vendrell, M.; Liu, X. *In Vivo* Tumor Visualization through MRI Off-On Switching of NaGdF_4 - CaCO_3 Nanoconjugates. *Adv. Mater.* **2019**, *31* (37), No. 1901851.

(30) Wang, W.; Feng, Z.; Li, B.; Chang, Y.; Li, X.; Yan, X.; Chen, R.; Yu, X.; Zhao, H.; Lu, G.; Kong, X.; Qian, J.; Liu, X. Er^{3+} Self-Sensitized Nanoprobes with Enhanced 1525 nm Downshifting Emission for NIR-IIb *in Vivo* Bio-Imaging. *J. Mater. Chem. B* **2021**, *9*, 2899–2908.

(31) Wang, H.; Zhang, M.; Zhang, L.; Li, S.; Li, L.; Li, X.; Yu, M.; Mou, Z.; Wang, T.; Wang, C.; Su, Z. Near-Infrared Light and PH-Responsive $\text{Au@Carbon/Calcium Phosphate}$ Nanoparticles for Imaging and Chemo-Photothermal Cancer Therapy of Cancer Cells. *Dalton Trans* **2017**, *46* (43), 14746–14751.

(32) Ding, B.; Shao, S.; Jiang, F.; Dang, P.; Sun, C.; Huang, S.; Ma, P. a.; Jin, D.; Kheraif, A. A. A.; Lin, J. MnO_2 -Disguised Upconversion Hybrid Nanocomposite: An Ideal Architecture for Tumor Microenvironment-Triggered UCL/MR Bioimaging and Enhanced Chemodynamic Therapy. *Chem. Mater.* **2019**, *31* (7), 2651–2660.



JACS Au
AN OPEN ACCESS JOURNAL OF THE AMERICAN CHEMICAL SOCIETY

Editor-in-Chief
Prof. Christopher W. Jones
Georgia Institute of Technology, USA

Open for Submissions 

pubs.acs.org/jacsau  ACS Publications
Most Trusted. Most Cited. Most Read.